

ON THE ELECTRICAL AND NUMERICAL PROPERTIES OF HIGH Q RESONANCES IN FREQUENCY SELECTIVE SURFACES

A. S. Barlevy and Y. Rahmat-Samii

Department of Electrical Engineering
University of California
Los Angeles, CA 90095-1594, USA

- 1. Introduction**
- 2. Solution Methodology—Revisited**
- 3. $1 - \lambda$ High Q Resonance**
 - 3.A Perfect Electric Conductors
 - 3.B Real Metals
- 4. $1/2 - \lambda$ High Q Resonance**
- 5. Numerical Aspects**
 - 5.A Stability Considerations
 - 5.B Grating Lobe Singularities
 - 5.C Consistency and Accuracy
- 6. Conclusion**

Acknowledgment

Appendix

References

1. INTRODUCTION

Frequency Selective Surfaces (FSS) are periodic screens that act as electromagnetic filters. They are typically used in dichroic reflectors [1] and radomes [2]. Ideally, at some frequencies an FSS completely reflects an incident plane wave, while at other frequencies the FSS is completely transparent to the incident plane wave. When designing an FSS to achieve a certain spectral response, many parameters can be adjusted, such as the dimensions of periodicity, element shape,

dielectric thickness and constant, and number of periodic screens. Due to the vector nature of the electric and magnetic fields, the frequency response depends on the angle of incidence as well as the polarization of the incident wave. For capacitive type FSS (surfaces composed of scattering elements as opposed to scattering apertures [3]), 100% reflection is possible only when the elements are resonating. One of the figures of merit of a resonance is the Quality factor, Q , which is defined as

$$Q = \frac{f_0}{\Delta f} \quad (\text{dimensionless}) \quad (1)$$

where f_0 is the center frequency, and Δf is the 3 dB bandwidth.

The main goal of this paper is to give an in-depth understanding of resonances in FSS which are very narrow band (extremely high Q) by revisiting two different FSS which have been previously analyzed in the literature [4, 5]. When the resonant bandwidth becomes extremely small, numerical simulation becomes difficult. We detail in this paper all the problems associated with modeling high Q resonances.

The FSS in [4] (shown in Fig. 1) exhibits an extremely high Q resonance when the dipole length is approximately 1λ . This FSS is the topic of Section 3. The FSS in [5] (see Fig. 8) also exhibits an extremely high Q resonance, but its high Q resonance occurs when the width of the element is about 0.5λ . This FSS is investigated in Section 4. The high Q resonances in both FSS are extremely dependent on the angle of incidence. The resonant bandwidth becomes identically 0 Hz (infinite Q) when the incident angle is normal. In both cases, the frequency sampling by the original authors was too coarse to properly capture the high Q resonances for near normal incidence. In this work, the frequency sampling rate is reduced to .01 Hz out of 14 GHz (1 part in a trillion) near the high Q resonances, in order for the high Q resonances to become apparent.

The reason why certain resonances are necessarily narrow band in their nature is discussed in great depth. The analysis in Section 3 and 4 shows that the high Q resonances can only appear in infinite FSS composed of perfect conductors. The effect of surface impedance on the narrow band resonances is shown in Section 3.B.

The numerical consequences of the high Q resonances on the solution accuracy is investigated in depth in Section 5. It is found that near high Q resonances, the problem becomes less well posed in the sense that the matrix condition number rises sharply. Higher resonant Q results in higher condition numbers. Within the numerical analysis

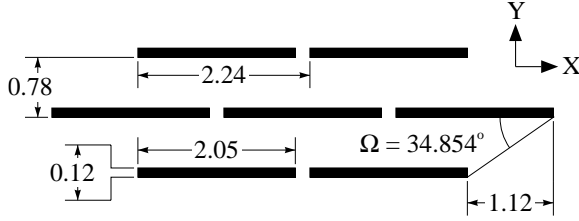


Figure 1. Section of a free standing infinite FSS of dipoles. Dimensions are in cm.; shaded region is metallic.

section, we explain why the matrix condition number increases near the high Q resonances. We also demonstrate that our results are still valid in spite of the fact that high condition numbers usually result in large numerical errors.

2. SOLUTION METHODOLOGY—REVISITED

The analysis of Frequency Selective Surfaces (FSS) is well documented in the literature [6]. Here, we present the final results, in order to emphasize certain numerical as well as physical aspects.

The solution involves a Method of Moments formulation [7] to solve an integral equation which takes into account the periodic nature of the problem. As usual in the Method of Moments, one solves a matrix equation of the following form:

$$\begin{bmatrix} z_{1,1} & \cdots & z_{1,N} \\ \vdots & & \vdots \\ z_{N,1} & \cdots & z_{N,N} \end{bmatrix} \cdot \begin{bmatrix} i_1 \\ \vdots \\ i_N \end{bmatrix} = \begin{bmatrix} v_1 \\ \vdots \\ v_N \end{bmatrix} \quad (2)$$

The unknown vector, $[i_1, i_2, \dots, i_N]^{\text{Transpose}}$, represent the current induced on a periodic cell, and the vector on the right hand side of (2) represents the integration of the incident field with the testing functions. The elements of the matrix in (2) have the form

$$z_{i,j}(\theta, \phi, f) = \sum_{m=1}^2 \sum_{p=-\infty}^{\infty} \sum_{q=-\infty}^{\infty} \frac{\eta_{mpq}}{2A} \iint \left(\left\{ \iint (\hat{k}_{mpq} \cdot \vec{B}_j(\vec{r}_{\mathbf{T}}')) e^{+j\vec{k}_{\mathbf{T}pq} \cdot \vec{r}_{\mathbf{T}}'} ds' \right\} \right)$$

$$\left(\hat{\mathbf{k}}_{mpq} \cdot \vec{T}_i(\vec{\mathbf{r}}_{\mathbf{T}}) \right) e^{-j\vec{\mathbf{k}}_{\mathbf{T}pq} \cdot \vec{\mathbf{r}}_{\mathbf{T}}} ds \quad (3)$$

where

- A is the area of the periodic cell

$$\begin{aligned} \vec{\mathbf{k}}_{\mathbf{T}pq} = & \left(\frac{2\pi p}{a} + k_0 \sin \theta \cos \phi \right) \hat{\mathbf{x}} \\ & + \left(\frac{2\pi q}{b} \hat{\mathbf{y}} - \frac{2\pi p}{a} \cot(\Omega) + k_0 \sin \theta \sin \phi \right) \hat{\mathbf{y}} \end{aligned}$$

with $k_0 = 2\pi f \sqrt{\mu\epsilon}$, θ and ϕ are the spherical coordinate angles of the direction of propagation of the incident field, a is the periodicity along the x -axis (2.24 cm in Fig. 1), b is the periodicity along the y -axis (0.78 cm in Fig. 1), and Ω is a measure of obliqueness (34.854° in Fig. 1).

- $\eta_{1pq} = \frac{\gamma_{pq}\eta}{k_0}$ (Transverse Magnetic, or TM case for $m=1$), $\eta_{2pq} = \frac{k_0\eta}{\gamma_{pq}}$ (Transverse Electric, or TE case for $m=2$), with $\eta = \sqrt{\frac{\mu}{\epsilon}}$

is the free space wave impedance, and $\gamma_{pq} = \sqrt{k_0^2 - |\vec{\mathbf{k}}_{\mathbf{T}pq}|^2}$ if

$$k_0 > |\vec{\mathbf{k}}_{\mathbf{T}pq}| \text{ or } \gamma_{pq} = -j\sqrt{|\vec{\mathbf{k}}_{\mathbf{T}pq}|^2 - k_0^2} \text{ if } k_0 < |\vec{\mathbf{k}}_{\mathbf{T}pq}|.$$

- $\vec{\mathbf{r}}_{\mathbf{T}} = x\hat{\mathbf{x}} + y\hat{\mathbf{y}}$ is the observation tangential coordinate, and $\vec{\mathbf{r}}_{\mathbf{T}}' = x'\hat{\mathbf{x}} + y'\hat{\mathbf{y}}$ is the source tangential coordinate.
- $\hat{\mathbf{k}}_{1pq} = \frac{\vec{\mathbf{k}}_{\mathbf{T}pq}}{|\vec{\mathbf{k}}_{\mathbf{T}pq}|}$ (TM case), and $\hat{\mathbf{k}}_{2pq} = \hat{\mathbf{z}} \times \hat{\mathbf{k}}_{1pq}$ (TE case). However, if $\theta = 0^\circ$ and $p = q = 0$, then $\hat{\mathbf{k}}_{1pq} = \cos \phi \hat{\mathbf{x}} + \sin \phi \hat{\mathbf{y}}$
- $\vec{B}_j(\vec{\mathbf{r}}_{\mathbf{T}}')$ is the j th basis functions and $\vec{T}_i(\vec{\mathbf{r}}_{\mathbf{T}})$ is the i th testing function.

Note that unlike the case of the non-periodic scatterers, for FSS, $z_{i,j}(\theta, \phi, f)$ in (3) is a function of the angles of incidence, $\{\theta, \phi\}$. The exponentials, $e^{-j\vec{\mathbf{k}}_{\mathbf{T}pq} \cdot \vec{\mathbf{r}}_{\mathbf{T}}}$ in (3) are called Floquet modes and they satisfy the periodic boundary condition that the scattered field in each cell be identical in magnitude, with a progressive phase shift due to the incident wave. The expression for the matrix elements in (3) is simplified for the case of no dielectrics.

Although numerical errors arise due to truncation of the infinite series in (3), in most cases no numerical errors are introduced due to the integration, since the integration can be performed analytically for a large class of basis and testing functions. The integrals in (3) are essentially Fourier transforms of the basis and testing functions. For

roof-top basis and testing functions (used throughout in this paper) the Fourier transform has the generic form of $\left(\frac{\sin(x)}{x}\right)^2 \cdot \left(\frac{\sin(y)}{y}\right)$ (assuming the function is triangular along the x -axis and constant along the y -axis).

Once the induced currents are found by inverting the matrix and dotting with the right hand vector in (2), the reflection coefficient can be found by integrating the induced current as such

$$\Gamma = \frac{\eta_{m,0,0}}{2A} \int_{\text{One Cell}} \int \left(\hat{\kappa}_{m,0,0} \cdot \vec{J}(\vec{\mathbf{r}}_{\mathbf{T}}') \right) e^{+j\vec{k}_{\mathbf{T}00} \cdot \vec{\mathbf{r}}_{\mathbf{T}}'} ds' \quad (4)$$

where $\vec{J}(\vec{\mathbf{r}}_{\mathbf{T}}')$ is the total induced current on the periodic element. The value of the subscript m in (4) is $m = 1$ for TM incidence, and $m = 2$ for TE incidence. Substitution of Euler's Identity into (4) ($e^{jx} = \cos(x) + j \sin(x)$ where $j = \sqrt{-1}$) yields

$$\Gamma = \frac{\eta_{m,0,0}}{2A} \int_{\text{One Cell}} \int \left(\hat{\kappa}_{m,0,0} \cdot \vec{J}(\vec{\mathbf{r}}_{\mathbf{T}}') \right) \cdot \left(\underbrace{\text{symmetric}}_{\cos(k_0 \mathcal{L} \sin \theta)} + j \underbrace{\text{anti-symmetric}}_{\sin(k_0 \mathcal{L} \sin \theta)} \right) dx' dy' \quad (5)$$

where

$$\mathcal{L} = x' \cos \phi + y' \sin \phi \quad (6)$$

By explicitly presenting Euler's Identity in the equation for the reflection coefficient as in (5), the symmetry properties of the integral can be more easily distinguished¹. Equation (5) shows that an anti-symmetric (odd) current distribution, \vec{J} , cannot radiate (have a non-zero reflection coefficient) at normal incidence ($\theta \equiv 0^\circ$). When $\theta \rightarrow 0^\circ$, but not identically zero, an odd current distribution can radiate, provided the magnitude of \vec{J} is sufficiently large.

A computer program to analyze FSS based on the Floquet mode expansion [6] was developed and tested. In the remainder of this paper,

¹ A symmetric (even) function is a function which satisfies $f(x) = f(-x)$, and anti-symmetric (odd) function is a function which satisfies $f(x) = -f(-x)$.

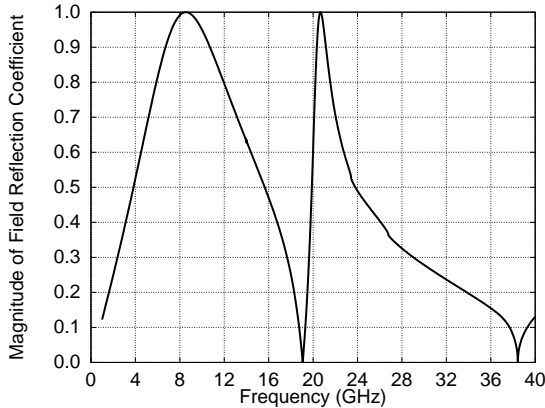


Figure 2. Field reflection coefficient of array in Fig. 1 illuminated by a normally incident plane wave with the E field polarized along the length of the dipoles.

we use this program to examine the physical and numerical properties of resonances in which the current distribution, \vec{J} in (5), is odd.

3. $1 - \lambda$ HIGH Q RESONANCE

3.A Perfect Electric Conductors

For the first example of high Q resonances, we revisit the FSS problem analyzed and measured by Larson and Munk [4]. The geometry and dimensions of this FSS are depicted in Fig. 1. The array is incident upon by a Transverse Electro-Magnetic (TEM) plane wave with the electric field polarized along the length of the dipoles. In Fig. 2 we show the magnitude of the field reflection coefficient along the specular direction. This result agrees with Figure 7 of [4]. Figure 2 shows two resonances. The first resonance, at 8.55 GHz, corresponds to a dipole length of $.58\lambda$, and the second resonance, at 20.65 GHz, corresponds to a dipole length of 1.41λ . At a first glance of Fig. 2, it seems that there is no resonance when the dipole length is approximately 1λ . Further analysis will prove otherwise.

Fig. 2 shows the reflection coefficient for the array in Fig. 1 under *normal incidence*. Fig. 3 shows what happens when the incident field is scanned along the length of the dipoles ($\phi = 0^\circ$) at frequencies for which the dipole length is approximately 1λ . As the incident angle,

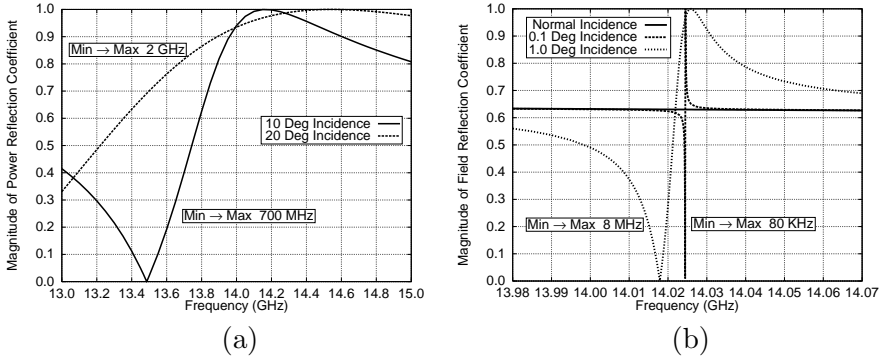


Figure 3. Field reflection coefficient of array in Fig. 1 at frequencies where dipole length near 1λ and the incident field is scanned along the length of the dipoles. (a) $\theta = 20^\circ, 10^\circ$, (b) $\theta = 1.0^\circ, 0.1^\circ, 0.0^\circ$. Min \rightarrow Max refers to the frequency separation between a reflection coefficient of 0 and 1. Note the different frequency scales, due to the different bandwidths.

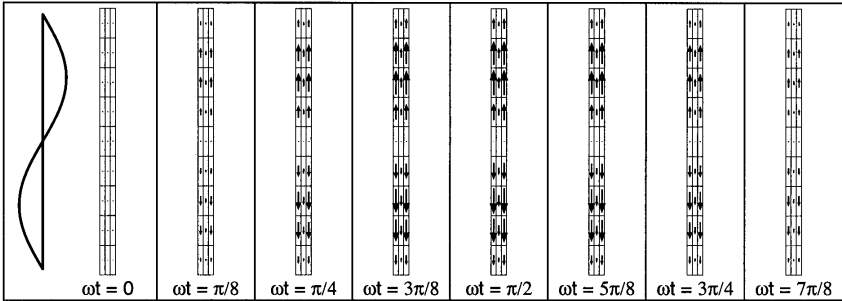


Figure 4 Time evolution of a vector plot of the induced $\text{Re}[e^{j\omega t} \vec{J}_s (\vec{r}_T')]$ at 1λ resonance. The magnitude of the current depends on the angle of incidence, as shown in Table 1.

θ , approaches 0° , the bandwidth of the resonance approaches 0 Hz. In fact, for small angles of incidence, the bandwidth is proportional to the square of the angle (reducing the angle by a factor of 10, reduces the bandwidth by a factor of 100).

A time evolution vector plot of the induced current is shown in Fig. 4. The advantage of presenting the currents in a time evolution vector plot is that in one graph (with eight sections) both the

magnitude and phase of both J_x and J_y can be shown at once. The plot of the induced currents in Fig. 4 helps explain why the bandwidth approaches 0 Hz as the incident angle, θ , approaches 0° . The resonant current (for the dipoles $\approx 1\lambda$) along the dipole length is an odd function (see figures in appendix for plots showing odd and even functions). For $\theta = 0^\circ$, complete symmetry exists so the integral in (5) vanishes. For $\theta \neq 0^\circ$, some radiation is possible, since there will not be an exact cancellation of the currents in the radiation integral (5). In order to obtain complete reflection though, the amplitude of the current must be large. As shown in Table 1, the magnitude of the current is approximately inversely proportional to θ for small θ . This is due to the fact that in (5), $\sin\theta \approx \theta$ for small θ . Since infinitesimally small θ results in infinitely large resonating currents, the bandwidth of such resonances tends to 0, as infinitely large currents are not physically possible.

Angle of Incidence	Condition Number	Max. Current Magnitude (A/m)
20.0°	1.5×10^4	0.107
10.0°	1.7×10^4	0.171
1.0°	6.4×10^5	1.536
0.1°	6.3×10^7	15.224

Table 1. Numerical results for 1λ resonance.

The high Q resonances in the FSS of Fig. 1 can also be explained by the reciprocal example of a radiating array. The total radiation pattern of the array is equal to the product of the element pattern times the array pattern. An odd current distribution gives an element pattern with a null at boresight (a difference pattern). For an infinitely large array, the array pattern is a delta function (or functions if grating lobes exist) in spherical coordinates. Therefore, if the array is not scanned (delta function at boresight), no radiation is possible (the product of a delta function and zero is zero). All the energy from the source will be returned as the input resistance of the array will be a perfect short. If the array is scanned by a small angle, some radiation will be possible, but only over a narrow bandwidth, as any match will be narrow band in nature due to the fact that the input resistance will be very small.

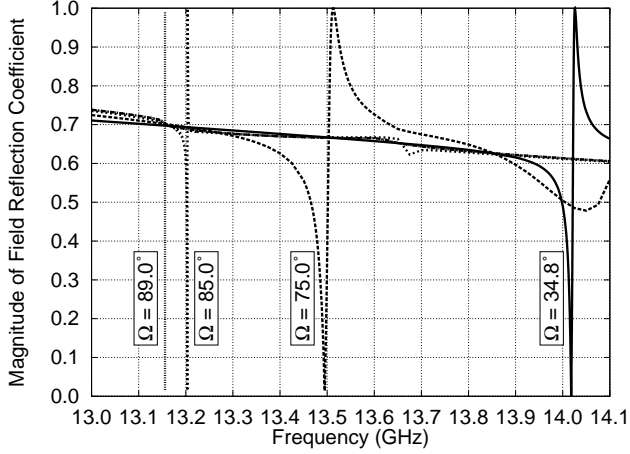


Figure 5. Reflection coefficient of array in Fig. 1 for different lattice angles, Ω . The direction of the incident plane wave is $\theta = 1.0^\circ$, $\phi = 0.0^\circ$. E field is polarized along the length of the dipoles.

Mode (p, q)	Cutoff Frequency	$\phi = \tan^{-1} \left(\frac{k_x}{k_y} \right)$
(0, 0)	0.0000 GHz	—
(-1, -1)	23.4186 GHz	$180^\circ + 34.854^\circ$
(-1, 0)	23.4186 GHz	$180^\circ - 34.854^\circ$
(1, 1)	23.4186 GHz	34.854°
(1, 0)	23.4186 GHz	-34.854°
(-2, -1)	26.7672 GHz	180.00°
(2, 1)	26.7672 GHz	0.00°
(0, -1)	38.4349 GHz	-90.00°
(0, 1)	38.4349 GHz	90.00°

Table 2. Cutoff frequencies and directions of propagations of higher order Floquet modes for FSS in Fig. 1 under normal incidence.

The dipoles in Fig. 1 can only resonate at 1λ if the lattice is not orthogonal ($\Omega \neq 90^\circ$). Figure 5 shows what happens to the 1λ resonance, at $\theta = 1.0^\circ$, as a function of the lattice angle Ω . As $\Omega \rightarrow 90^\circ$,

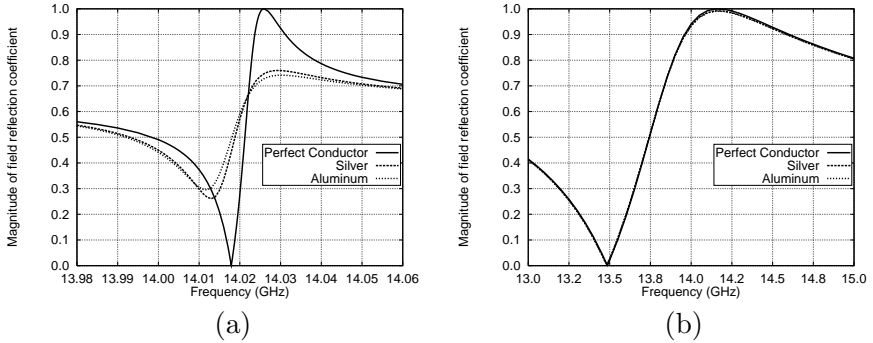


Figure 6. 1λ resonance for FSS in Fig. 1 composed of metals with different surface impedance. (a) $\theta_{\text{inc}} = 1^\circ$, (b) $\theta_{\text{inc}} = 10^\circ$. Note the different frequency scales, due to the different bandwidths.

the resonance is pushed down in frequency and the bandwidth is narrowed. For $\Omega = 90^\circ$, the 1λ resonance completely vanishes. The reason for that lies in the cutoff frequency of the higher order Floquet modes. As the lattice angle, Ω , increases to 90° , the cutoff frequency for the $\{p = \pm 1, q = 0\}$ Floquet mode (see Table 2) reduces from 23.42 GHz to 13.38 GHz. The frequency downshift of the grating lobe suppresses the 1λ resonance as the propagating grating lobe takes energy away from the dominant (or specular) mode (the resonance is 100% reflection of the dominant mode).

3.B Real Metals

With the FSS composed of PEC, it was shown that in the limit of normal incidence ($\theta \rightarrow 0.0^\circ$) the current can be made arbitrarily large, resulting in an arbitrarily narrow bandwidth resonance. The PEC can support arbitrarily large currents, because there is no dissipation in a perfect conductor. Real metals, having a finite non-zero resistivity, cannot support arbitrarily large currents, as they dissipate power.

It is possible to model the response of an FSS composed of real metallic scatterers, as opposed to PEC, by using the impedance boundary condition

$$\vec{E}_{\text{tangential}}(\vec{\mathbf{r}}_{\mathbf{T}}') = Z_s \vec{J}(\vec{\mathbf{r}}_{\mathbf{T}}') \quad (7)$$

rather than $\vec{E}_{\text{tangential}}(\vec{\mathbf{r}}_{\mathbf{T}}') = 0$ [5]. The term Z_s is known as the surface impedance, and it is given by

$$Z_s = (1 + j) \sqrt{\frac{\pi \mu f}{\sigma}} \left(\frac{\Omega}{\text{square}} \right) \quad (8)$$

At 14 GHz, the surface impedance of silver is $Z_s = .030(1 + j) \frac{\Omega}{\text{square}}$ and for aluminum it is $Z_s = .037(1 + j) \frac{\Omega}{\text{square}}$ [9].

The effect of the surface impedance on the MoM solution is to give an additional term to the left hand side of (3) such that

$$z_{i,j} \rightarrow z_{i,j} + Z_s \iint \text{Basis}_i(x, y) \cdot \text{Testing}_j(x, y) dx dy \quad (9)$$

Because of the use of subdomain basis and testing functions, the integral in (9) vanishes for most combinations of i and j . The integral is non-zero only when a basis function overlaps a testing function and their vector dot product is not zero. The self element is the matrix element most affected by the non-zero surface impedance.

The results for the FSS in Fig. 1 composed of metals with different surface impedance is shown in Fig. 6. In Fig. 6a, the maximum current amplitude (for the PEC FSS) is 1.54 A/m (see Table 1). This is why the introduction of a surface impedance by silver and aluminum (small as it may be) causes a large change in the reflection coefficient. On the other hand, in Fig. 6b, the maximum current amplitude (for the PEC FSS) is .17 A/m. Therefore, there is not much difference in the reflection coefficient between the PEC FSS and the FSS made of aluminum and silver when the incident angle, θ , is 10° .

Finally, Fig. 7 shows the result of the measurement of the transmission coefficient performed by Larson [10] on the FSS in Fig. 1 composed of slots instead of patches. As stated in [10], the array was misaligned by 3° and that gave rise to the resonance at 14 GHz (the misalignment has the same effect as scanning the incident field). Because the ground plane was not a PEC (or a superconductor), the resonance was dampened and full transmission was not seen in the measurement.

4. $1/2 - \lambda$ HIGH Q RESONANCE

We will now show another example of a high Q resonance. In this example, the resonance occurs when the width of the periodic element, as shown in Fig. 8, is approximately $\lambda/2$. We use the term “width” to refer to the direction perpendicular to the polarization of the incident

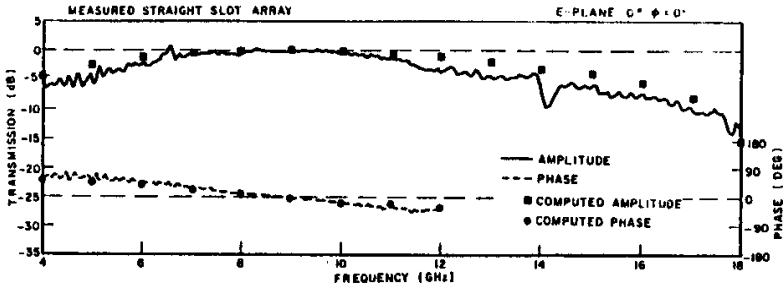


Figure 7. Measured transmission coefficient of the complementary slot type FSS in Fig. 1. Array was misaligned by 3° . Reprinted from [10].

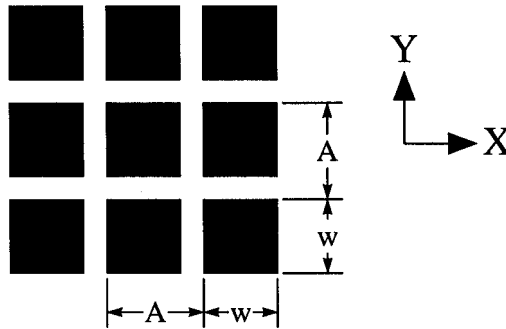


Figure 8. Section of an infinite free standing square FSS. Shaded region is metallic.

field, whereas in the previous section we used the term “length” to refer to the direction aligned with the polarization of the incident field. In Fig. 9, we plot the specular field reflection coefficients of the FSS in Fig. 8 for four different w/A ratios under $\theta = 1^\circ$, $\phi = 0^\circ$ Transverse Electric (TE) illumination (E field is y polarized). In the previous example of section 3, we demonstrated the effect of the incident angle on the high Q resonance. For this example, we would like to demonstrate the effect of the resonant frequency on the high Q resonance.

Fig. 10 shows a closeup of Fig. 9 at the $\lambda/2$ resonance for each w/A ratio. Increasing the size of the periodic element with respect to the periodic cell causes a downshift in the resonant frequency. This reduces the resonant wave number, k_0 , in (5). Since k_0 inside the sine term in (5) is smaller, the magnitude of the induced odd current increases, and hence the bandwidth must decrease. This is shown in

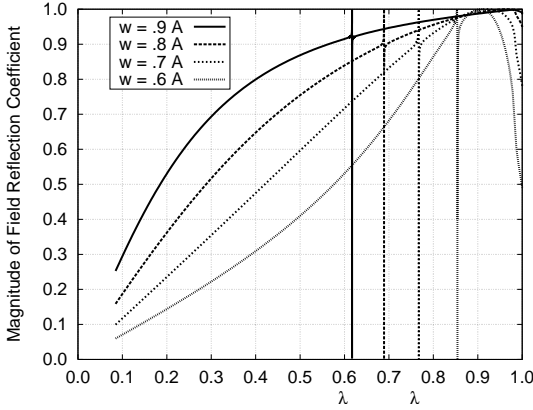


Figure 9. Reflection coefficient of FSS in Fig. 8 for different ratios of w/A . The FSS is illuminated by a TE plane wave of incident angles $\theta = 1.0^\circ$, $\phi = 0.0^\circ$.

Fig. 10. When $w/A = .6$ (Fig. 10a), the separation between full reflection and full transmission is $.001017A/\lambda$ (0.12% bandwidth). As the resonance frequency is reduced to $.617A/\lambda$ at $w/A = .9$ (Fig. 10d), the separation between full reflection and full transmission reduces to $.000051A/\lambda$ (0.008% bandwidth).

The surface current induced on the FSS at the $\lambda/2$ resonance is shown as a time evolution vector plot in Fig. 11. The scale in Fig. 11 is such that the largest arrow represents $J_s = .06$ Amps/m. We have specifically plotted $w/A = 0.6$ so the even mode can be seen at $\omega t = 0$ as well as the odd mode at $\omega t = \pi/2$. More information about the current modes can be found in the appendix.

Because the incident field is polarized along the y -axis, the J_x component in this case is the cross-pol. Due to the symmetry about the $y = 0$ line (the incident field is scanned along $\phi = 0^\circ$), integration of J_x is almost zero (100 dB less than the co-pol). In the 1λ resonance of the previous example, the current was zero at the dipole ends (see Fig. 4). In this example, J_y in Fig. 11 approaches $\pm\infty$ at $x = \pm w/2$. By observing the current at $\omega t = \pi/8, \pi/4, 5\pi/8, 3\pi/4$, one can see that the phase of J_y is not exactly 180° between the left side and the right side. The slight asymmetry in J_y can be supported by the asymmetry (due to the 1° scan) about $x = 0$.

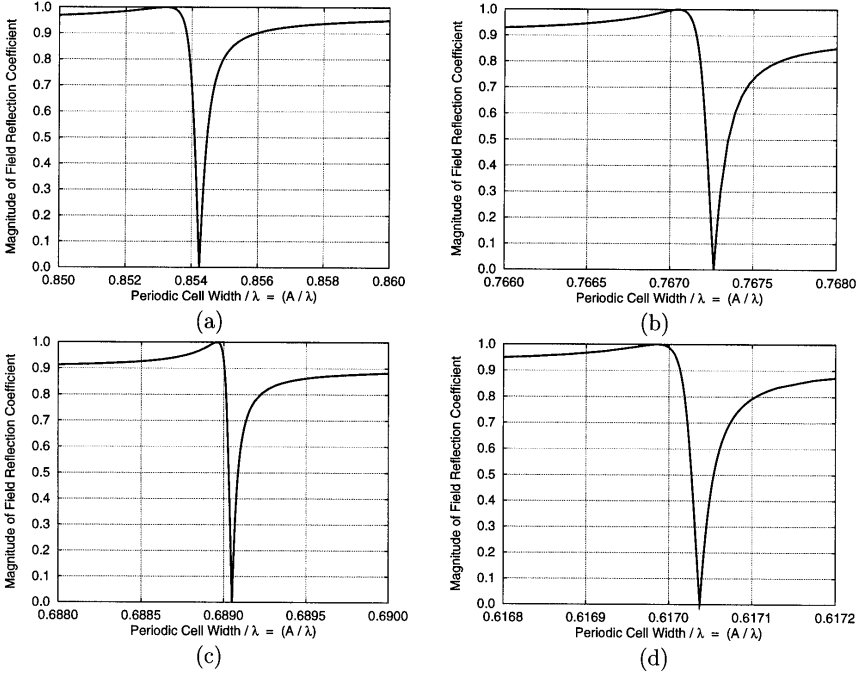


Figure 10. Close up of Fig. 9 at the $\lambda/2$ resonance. (a) $w/A = .6$, (b) $w/A = .7$, (c) $w/A = .8$, (d) $w/A = .9$.

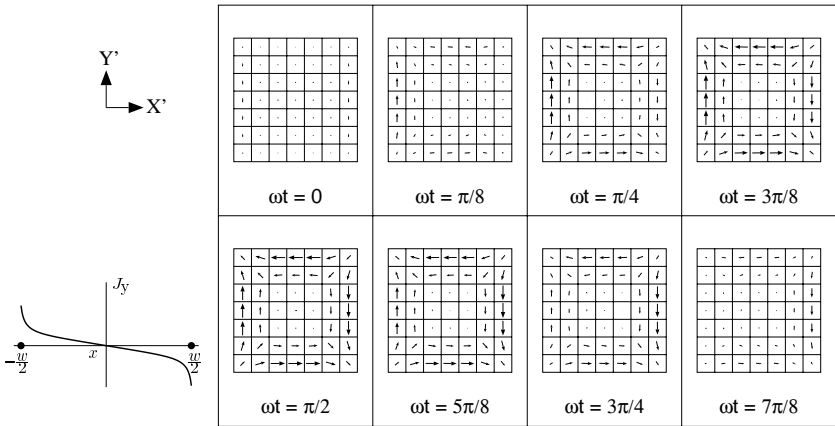


Figure 11. Time evolution of a vector plot of the induced $\Re[e^{j\omega t} \vec{J}_s]$ (\vec{r}_T') at $\lambda/2$ resonance. The current shown is for $w/A = 0.6$.

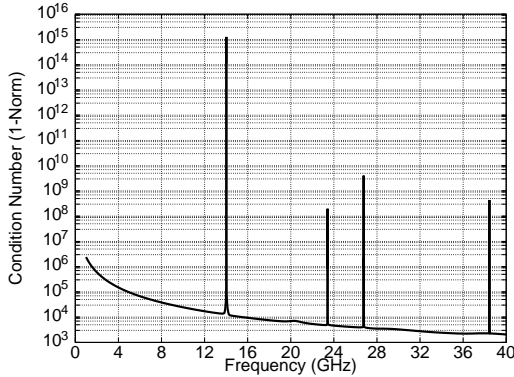


Figure 12. Condition number for the matrix used to obtain the results in Fig. 2. The size of the matrix is 54×54 and it contains coefficients for both J_x and J_y . The vertical scale is logarithmic.

5. NUMERICAL ASPECTS

A condition number [11] is a figure of merit for the singularity of a matrix. Higher condition numbers indicate that the matrix, such as the one in Eq. (2), is not well-posed. For singular matrices ($\det[\tilde{\mathbf{Z}}] \equiv 0$) the condition number is infinite. It is a well known fact that the round-off errors in the solution of the unknown variables are proportional to the condition number.

Figure 12 shows the 1-Norm condition number [11] of the MoM matrix used in calculating the results of Fig. 2. There are four frequencies in Fig. 12 for which the condition number increases very rapidly. In the scale of Fig. 12, the increases appear as sharp “spikes”, but on a finer scale, as in Fig. 13, the increase is smooth. The first “spike” in Fig. 12, near 14 GHz, is due to the zero bandwidth (infinite Q) 1λ resonance discussed in Section 3. The three other “spikes” occur at the cutoff frequencies of higher order Floquet modes (grating lobes).

Theoretically, the “spikes” in Fig. 12 should increase to infinity (i.e., singular matrix) for all four cases. The reason the condition number is not infinite is that the matrix is singular only at discrete frequencies which require infinite number of digits to specify (in some cases, the dimensions of the periodicity of the FSS might allow the cutoff frequency of higher order Floquet modes to be specified by a finite number of digits; in such a case, numerical simulation is not possible at the exact cutoff frequency). Therefore, due to the finiteness of a

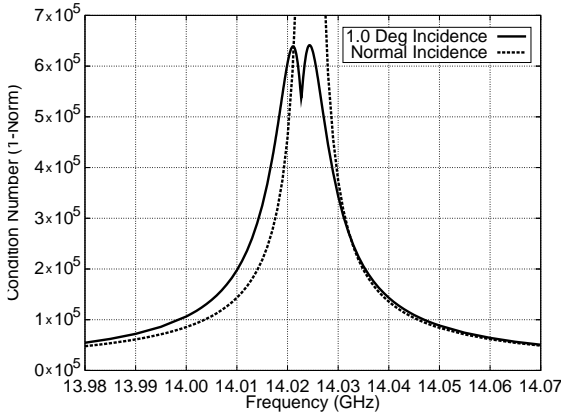


Figure 13. Matrix condition number for array in Fig. 1 where dipole is length near 1λ for two different angles of incidence.

digital computer, the condition number cannot be infinite. The reason the first “spike” *appears* to be higher than the other “spikes” is that it approaches infinity faster. As a result, using equal frequency sampling (.01 Hz near the “peak”) results in a higher condition number for the first “spike”.

5.A Stability Considerations

In order for a physical problem to be well-posed (well conditioned), it must satisfy three conditions. The three conditions, which together are sufficient for well-posedness [12], are:

1. Existence.
2. Uniqueness.
3. Continuous dependence of the solution on the data.

The last condition is a condition of stability, i.e., a small change in the data should causes only a small change in the solution.

For high Q resonances (such as the $1 - \lambda$ resonance shown in Fig. 3b) a small frequency change results in a large change in the reflection coefficient (as well as the current induced on the FSS, but it is not easy to plot the current distribution as a function of frequency). The narrower the bandwidth, the larger the change in the response for the same change in frequency. Therefore, as shown in Table 1, as the incident angle, θ , approaches 0° (the resonance bandwidth ap-

proaches 0 Hz), the condition number approaches infinity (see section 2 regarding the dependence of the $\tilde{\mathbf{Z}}$ matrix on the incident angle). It can also be seen in Table 1 that for small θ , the condition number is inversely proportional to θ^2 . Figure 13 shows that the condition number has an upper bound for $\theta = 1^\circ$, but no such upper bound exists for $\theta = 0^\circ$. The first maximum of the $\theta = 1^\circ$ curve in Fig. 13 occurs at the cross-over frequency where the condition number of $\theta = 1^\circ$ equals the condition number of $\theta = 0^\circ$. The second maximum of the $\theta = 1^\circ$ curve occurs at the frequency where the matrix is singular in the $\theta = 0^\circ$.

From a numerical standpoint, the ill-posedness can be explained by considering the determinant of the matrix (the higher the condition number, the smaller the determinant). The inverse matrix is inversely proportional to the determinant. In general, as the magnitude of the elements of the inverse matrix is increased, the magnitude of the current also increases (the exact magnitude of the current depends on the excitation vector on the right hand side of (2)). As mentioned in Sections 3, 4, and the appendix, the magnitude of the induced current approaches infinity as the resonant bandwidth approaches 0 Hz. The only way for the current magnitude to rapidly change with frequency while the elements of the matrix only gradually change with frequency is for the matrix determinant to approach 0 rapidly.

5.B Grating Lobe Singularities

As previously mentioned, the three “spikes” at 23.4 GHz, 26.8 GHz, and 38.4 GHz in Fig. 12 are due to higher order Floquet modes (grating lobes) starting to propagate (see Table 2). The question “why is the matrix singular at the onset of grating lobe propagation?” can be answered both physically and numerically. The numerical answer is that all the elements of the matrix in (2) become infinite because η_{2pq} in (3), becomes infinite at the cutoff frequency of the $\{p, q\}$ mode (γ_{pq} is zero at the cutoff frequency). The physical answer requires a close examination of Fig. 2. Figure 14 shows a close-up of Fig. 2 at the onset frequencies for grating lobe propagation. At all three frequencies, the derivative (with respect to frequency) of the reflection coefficient is infinite (vertical) at the grating lobe cutoff frequency. When the derivative of the solution with respect to frequency is large, a small change in the frequency results in a large change in the

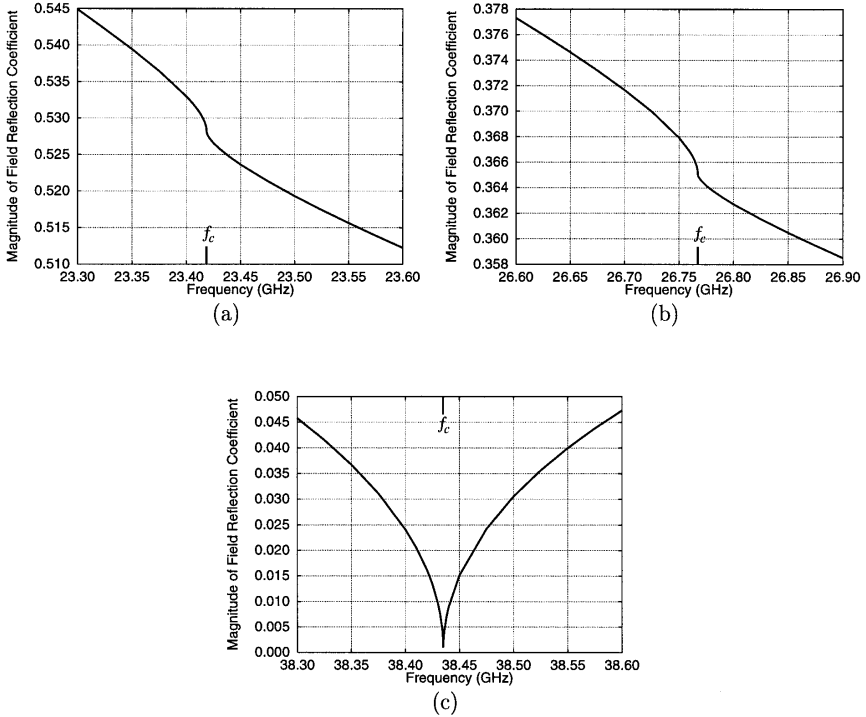


Figure 14. Close up of Fig. 2 near the cutoff frequencies of higher order Floquet modes (see Table 2 for mode indices and their corresponding cutoff frequencies).

solution. Hence, the solution is not continuously dependent on the data, resulting in an ill-conditioned matrix.

The reason the derivative of the solution with respect to frequency is infinite near the onset of grating lobes can be found by looking at the propagation constant, γ , of a given Floquet mode, defined as

$$\gamma = \alpha + j\beta = \frac{2\pi}{c} \begin{cases} \sqrt{f_c^2 - f^2} & f \leq f_c \\ j\sqrt{f^2 - f_c^2} & f \geq f_c \end{cases} \quad (10)$$

where f_c is the cutoff frequency for the given mode. A plot of (10) is shown in Fig. 15, which shows that

$$\lim_{f \rightarrow f_c^-} \frac{\partial \gamma}{\partial f} = \infty \quad \text{and} \quad \lim_{f \rightarrow f_c^+} \frac{\partial \gamma}{\partial f} = j\infty \quad (11)$$

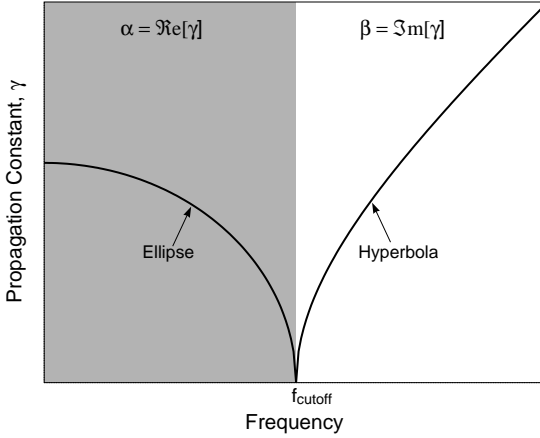


Figure 15. Plot of propagation constant, γ , for an arbitrary Floquet mode. Below the cutoff frequency γ is real (evanescent waves), and above the cutoff frequency γ is imaginary (propagating waves).

Due to the linearity of Maxwell's equations, if the derivative with respect to frequency of one Floquet mode, $e^{\gamma z}$, is infinite at some frequency, then the solution (given in this paper as the reflection coefficient) at that frequency must also have an infinite derivative with respect to frequency.

It is worth mentioning here that under some circumstances, the FSS problem will not be ill-conditioned at a grating lobe cutoff frequencies. The plot of the condition number in Fig. 12 is for a matrix with coefficients for both unknown J_x and unknown J_y . It was found that the condition number shows no appreciable rise at 26.7672 GHz (the cutoff frequency for $\{p = \pm 2, q = \pm 1\}$ Floquet modes) for a matrix of only J_x coefficients (J_y is negligible for thin dipoles). The reason the problem is well conditioned when only solving for the x component of the current is that the grating lobes $\{p = \pm 2, q = \pm 1\}$ propagate in the direction of $\phi = 0^\circ, 180^\circ$ (see Table 2), which is along the x axis. This causes cancellation of vector dot product of $(\hat{\kappa}_{2pq} \cdot \vec{T}_i(\vec{\mathbf{r}}_{\mathbf{T}}))$ in (3), since the testing functions have only a \hat{x} component, while $\hat{\kappa}_{2pq}$ only has a \hat{y} component. Therefore, the matrix with only J_x coefficients is oblivious to the $\{p = \pm 2, q = \pm 1\}$ Floquet modes. In general, though, the matrix is ill-conditioned at cutoff frequencies of all higher order Floquet modes.

Frequency (Hz)	Reflected Power		Reflected Phase		Condition Number
	LU Matrix	Inverse Matrix	LU Matrix	Inverse Matrix	
14,000,000,000.00	39.94%	39.94%	129.199°	129.199°	85,502
14,010,000,000.00	39.84%	39.84%	129.140°	129.140°	143,341
14,020,000,000.00	39.74%	39.74%	129.081°	129.081°	459,096
14,024,485,227.63	39.70%	39.71%	129.054°	129.048°	1,268,288,115,110,644
14,030,000,000.00	39.64%	39.64%	129.022°	129.022°	374,314

Table 3. Results for Fig. 2 when dipole length is near 1λ .

Frequency (Hz)	RMS Residue of LHS of (12)	RMS Residue of LHS of (13)	Condition Number
14,000,000,000.00	6.484×10^{-13}	4.913×10^{-13}	85,502
14,010,000,000.00	9.915×10^{-13}	5.391×10^{-13}	143,341
14,020,000,000.00	3.500×10^{-12}	7.142×10^{-13}	459,096
14,024,485,227.63	7.755×10^{-3}	8.896×10^{-4}	1,268,288,115,110,644
14,030,000,000.00	2.570×10^{-12}	6.471×10^{-13}	374,314

Table 4. Residues of (12) and (13) near the first “spike” of Fig. 12.

5.C Consistency and Accuracy

When the condition number is high, the accuracy of the solution comes into question. We will therefore pay attention to the accuracy of the solution with the aid of Tables 3 and 4. Table 3 shows that when the condition number exceeds 10^{15} , the two solutions, using LU (lower upper) matrix decomposition [11] or the inverse matrix directly, differ in the third digit. While not shown explicitly in the table, when the condition number is less than 10^6 , the two solutions agree to at least 12 digits.

Two methods that allow direct examination of the accuracy of the inverse matrix are [13]:

$$\frac{1}{z_{\text{avg}}} \left(\tilde{\mathbf{Z}} - \left((\tilde{\mathbf{Z}})^{-1} \right)^{-1} \right) = \tilde{\mathbf{0}} \quad (12)$$

$$\tilde{\mathbf{Z}} \cdot \tilde{\mathbf{Z}}^{-1} - \tilde{\mathbf{I}} = \tilde{\mathbf{0}} \quad (13)$$

where $\tilde{\mathbf{Z}}$ is the matrix to be tested, $\tilde{\mathbf{I}}$ is the identity matrix, and z_{avg} is the average magnitude of the elements in the matrix. The reason for

dividing by z_{avg} in (12) is to make the left hand side unitless so that the residue will not depend on the magnitude of the matrix elements. Table 4 shows the Root Mean Square (RMS) of the elements of the residue matrices on the left hand side of (12) and (13). As expected, when the condition number increases by 10 orders of magnitude, the accuracy of the inverse matrix, as indicated by the size of the residues in Table 4, decreases by 10 orders of magnitude. Finer sampling of the frequency would yield even higher condition numbers, which would cause the inverse matrix to be even less accurate. The reason the residues in Table 4 are on the order of 10^{-13} for condition numbers less than 10^6 is the use of double precision arithmetics in calculating the matrix elements. Had single precision arithmetics been used, the residues in Table 4 would have been 9 orders of magnitude higher and the solution at 14,024,485,227.63 Hz would have been highly inaccurate.

The exact frequency for which the condition number rises is very sensitive to the truncation of the summation in (3). The data in Tables 3 and 4 are the results when both p and q are summed from -30 to $+30$.

6. CONCLUSION

The goal of this work was to expose the existence of infinitely high Q resonances in infinitely periodic screens. The narrow band resonances occur when the induced current distribution on the elements of the FSS has odd symmetry. An individual element with an odd current distribution radiates a difference pattern with a deep null at boresight. In the environment of an unscanned infinite array, which is the case of an FSS under normal incidence, the array pattern is a delta function (infinite gain) at boresight. The total radiation is the product of the array pattern with the element pattern. Since the element with a difference pattern cannot radiate at boresight, there can be no resonance (the resonance bandwidth becomes 0 Hz) when the incident plane wave is normal to the FSS (no scan).

When the incident field is scanned, it is possible for the FSS elements to radiate, and hence the FSS can resonate. However, the resonance is not very efficient, hence it is narrow band. High frequency sampling in numerical simulations is required in order to properly capture high Q resonances. Otherwise, the resonance might not appear in the results.

The narrow band resonance is sustained by very large currents. This is not a problem for perfect conductors, but real metals have finite

surface resistance and hence dissipate power. This was shown to dampen high Q resonances to a point where they are not practical with conductors such as silver and aluminum.

Numerically, when the resonance bandwidth is very small, finding the response of the FSS becomes an ill-posed problem. The ill-posedness comes about from the loss of stability, in the sense that a small change in frequency results in a large change in the induced current. The inverse of an ill-posed (ill-conditioned) matrix is usually not numerically accurate, but the use of double precision arithmetic can help mitigate numerical errors. Singularities due to loss of stability were also shown to occur in the FSS problem at cutoff frequencies of higher order Floquet modes.

While the high Q resonances can impact a numerical simulation, they most likely have little practical implications unless the FSS is composed of superconductors, since regular metals were shown in this paper to dampen the high Q resonances. Superconducting FSS have been investigated in [14]. While ohmic losses of real metals dampen high Q resonances, the dampening might not be enough to completely obliterate the high Q resonances in practice. A measurable ripple, as shown by measurements in [10], might still exist.

ACKNOWLEDGMENT

The authors would like to thank Dr. Clay Larson of Lockheed Martin (Palmdale, California), Mr. Mats Gustafsson of Lund University (Sweden), and Dr. Yehuda Leviatan of the Technion (Israel) for their useful discussions. This work was supported in part by the U.S. Army Research Office under Contract DAAH04-96-1-0389.

APPENDIX

In Section 3 and 4 we plots of the induced current (Fig. 4 and Fig. 11) and note that the current has an odd (anti-symmetric) distribution. A more rigorous analysis of the current distribution can be done by decomposing the current into resonating modes. In this paper, rooftop functions, which are subdomain, are used as the basis and testing functions in the MoM to find the induced currents. We will now re-expand the current in term of global resonating modes (entire domain functions).

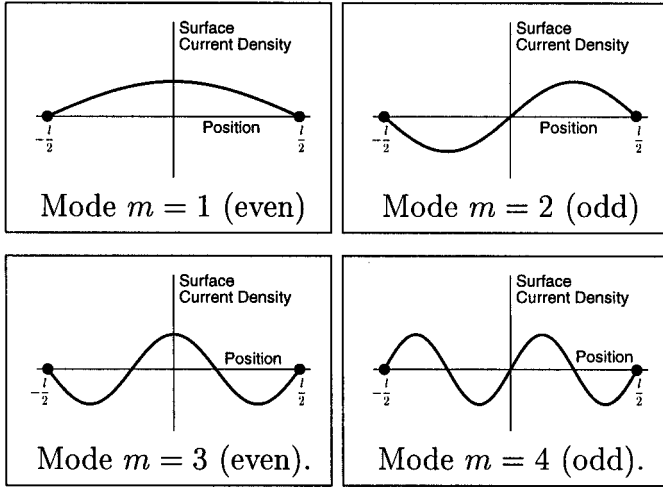


Figure A1. Plots of the first four expansion modes in (A.1).

For the dipoles of Section 3, the x component of the current is re-expanded along the length of the dipole such that the current is zero at the edge (see Fig. A1). Specifically,

$$\begin{aligned}
 J_x(x') = & \sum_{m=1,3,5,7,\dots} a_m \cos\left(\frac{m\pi x'}{2(l/2)}\right) \\
 & + \sum_{m=2,4,6,8,\dots} a_m \sin\left(\frac{m\pi x'}{2(l/2)}\right).
 \end{aligned} \tag{A.1}$$

where $J_x(x')$ is the induced current determined by the rooftop expansion in the MoM. The unknown coefficients, a_m , can be found by exploiting the orthogonality of the sine and cosine functions. Specifically, this is achieved by integrating the product of $J_x(x')$ (which is given as a sum of rooftop functions) with the particular mode of interest.

Table A.1 shows the magnitude and phase of the first three coefficients of (A.1) for the 1λ resonance and anti-resonance under different angles of incidence. There are a few interesting facts that are revealed upon close examination of Table A.1.

- The even modes are in phase quadrature with the odd modes. This is due to the j in (5).

- The even modes are not as sensitive as the odd mode to frequency (resonance as opposed to anti-resonance) and angle of incidence.
- The magnitude of the odd mode is approximately inversely proportional to θ , and the frequency difference between resonance (reflection) and anti-resonance (transmission) is approximately proportional to θ^2 . This was discussed in Section 3.
- There is no contradiction between Table A.1 and Table 1. The former shows only the magnitude of the first three a_m coefficients of (A.1) whereas the latter shows the magnitude of the total current.

Angle of Incidence θ (Deg)	Frequency (GHz)	Status	Mode $m = 1$ (Even) (A/m)		Mode $m = 2$ (Odd) (A/m)		Mode $m = 3$ (Even) (A/m)	
			Mag	Phase	Mag	Phase	Mag	Phase
0.1°	14.02442	Transmission	0.040	-91.0°	13.080	-0.5°	0.013	-92.9°
0.1°	14.02450	Reflection	0.039	0.4°	15.894	-90.2°	0.001	148.9°
1.0°	14.01790	Transmission	0.040	-90.1°	1.297	-0.1°	0.013	-90.3°
1.0°	14.02590	Reflection	0.038	0.4°	1.603	-89.6°	0.001	177.2°
10.0°	13.48500	Transmission	0.042	-89.9°	0.143	0.6°	0.010	-90.0°
10.0°	14.18500	Reflection	0.039	-1.8°	0.169	-91.8°	0.000	175.0°
20.0°	12.54000	Transmission	0.043	-90.2°	0.085	-0.2°	0.004	-90.3°
20.0°	14.54000	Reflection	0.035	0.1°	0.109	-89.9°	0.001	0.3°

Table A.1. Current modes for 1λ resonance and anti-resonance of FSS in Fig. 1. $\phi_{\text{inc}} = 0^\circ$.

Also note that anti-resonance (full transmission) is achieved when the radiation from the even modes *cancel*s the radiation from the odd modes. At resonance, the odd and even modes add together to give 100% reflection.

For the wide patches of Section 4, the y component of the current is re-expanded along the width of the patch (x direction – perpendicular to the polarization of the induced current electric field), such that the current approaches infinity at the edge. (see Fig. A2). Specifically,

$$\begin{aligned}
 J_y(x') = & \sqrt{\frac{1}{1 - \left(\frac{x'}{w/2}\right)^2}} \left(\sum_{m=1,3,5,7,\dots} a_m \sin\left(\frac{m\pi x'}{2(w/2)}\right) \right. \\
 & \left. + \sum_{m=0,2,4,6,\dots} a_m \cos\left(\frac{m\pi x'}{2(w/2)}\right) \right). \tag{A.2}
 \end{aligned}$$

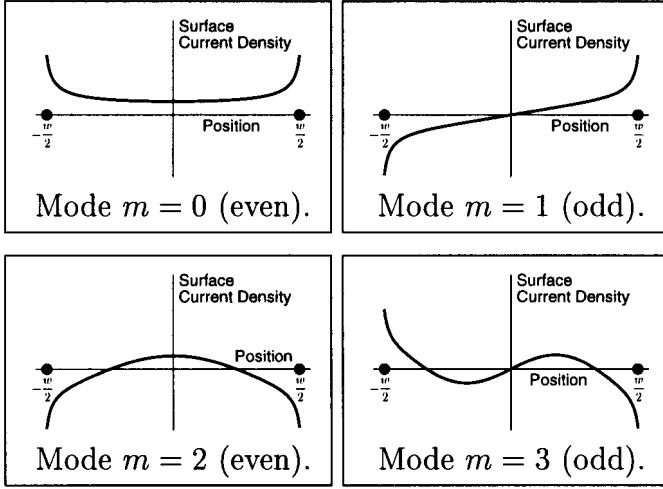


Figure A2. Plots of the first four expansion modes in (A.2).

w/A	A/λ	Status	Mode $m = 0$ (Even) (A/m)		Mode $m = 1$ (Odd) (A/m)		Mode $m = 2$ (Even) (A/m)	
			Mag	Phase	Mag	Phase	Mag	Phase
0.9	0.61699	Reflection	0.011	0.0°	0.255	90.0°	0.002	180.0°
0.9	0.61705	Transmission	0.009	-89.8°	0.603	0.2°	0.010	90.2°
0.8	0.68897	Reflection	0.012	0.0°	0.215	90.0°	0.002	180.0°
0.8	0.68906	Transmission	0.006	-89.9°	0.441	0.1°	0.007	90.1°
0.7	0.76706	Reflection	0.013	0.0°	0.148	90.0°	0.002	180.0°
0.7	0.76728	Transmission	0.004	-90.0°	0.309	0.0°	0.006	90.0°
0.6	0.85323	Reflection	0.015	0.0°	0.057	90.0°	0.002	180.0°
0.6	0.85425	Transmission	0.002	-89.9°	0.184	0.1°	0.005	90.1°

Table A.2. Current modes for $\frac{1}{2}\lambda$ resonance and anti-resonance of FSS in Fig. 8. $\theta_{\text{inc}} = 1.0^\circ$.

Again, $J_y(x')$ is the current that was determined by the MoM. The way to calculate the a_m coefficients in (A.2) is slightly different from the method used for calculating the coefficients in (A.1). The difference is that with (A.2), both sides of the equation must first be multiplied by the factor $\sqrt{1 - \left(\frac{x'}{w/2}\right)^2}$. The rest is the same. The principal effect of the extra multiplication is that the integration must be done numerically, whereas the a_m coefficients in (A.1) can be found analytically.

Table A.2 shows the first three a_m expansion coefficients of (A.2) for the high Q $\lambda/2$ resonance of Fig. 10. The coefficients are given for different ratios of w/A . All the conclusions reached for Table A.1 can be applied to Table A.2 except that Table A.2 emphasizes the behavior of the odd modes for different resonant frequencies rather than different angles of incidence.

REFERENCES

1. Rahmat-Samii, Y., and A. N. Tulintseff, "Diffraction analysis of frequency selective reflector antennas," *IEEE Trans. Antennas Propagat.*, Vol. AP-41, No. 4, 476–487, Apr. 1993.
2. Chu, R. S., "Analysis of an infinite phased array of dipole elements with RAM coating on ground plane and covered with layered radome," *IEEE Trans. Antennas Propagat.*, Vol. AP-39, No. 2, 164–176, Feb. 1991.
3. Zarrillo, G., and K. Aguiar, "Closed-form low-frequency solutions for electromagnetic waves through a frequency selective surface," *IEEE Trans. Antennas Propagat.*, Vol. AP-35, No. 12, 1406–1417, Dec. 1987.
4. Larson, C. J., and B. A. Munk, "The broad-band scattering response of periodic arrays," *IEEE Trans. Antennas Propagat.*, Vol. AP-31, No. 3, 261–267, Mar. 1983.
5. Cwik, T. A., and R. Mittra, "Scattering from a periodic array of free-standing arbitrarily shaped perfectly conducting or resistive patches," *IEEE Trans. Antennas Propagat.*, Vol. AP-35, No. 11, 1226–1234, Nov. 1987.
6. Montgomery, J. P., "Scattering by an infinite periodic array of thin conductors on a dielectric sheet," *IEEE Trans. Antennas Propagat.*, Vol. AP-23, No. 1, 70–75, Jan. 1975.
7. Harrington, R. F., *Field Computation by Moment Methods*, MacMillan, New York, 1968.
8. Imbriale, W. A., V. Galindo-Israel, and Y. Rahmat-Samii, "On the reflectivity of complex mesh surfaces," *IEEE Trans. Antennas Propagat.*, Vol. AP-39, No. 9, 1352–1365, Sep. 1991.
9. Balanis, C. A., *Advanced Engineering Electromagnetics*, New York, John Wiley & Sons, 1989.
10. Larson, C. J., "The Broadband Frequency Response of Periodic Surfaces," Ph.D. dissertation, Dept. Elect. Eng., Ohio State Univ. Columbus, Mar. 1980.
11. Golub, G. H., and C. F. Van Loan, *Matrix Computations*, 2nd ed., Baltimore, MD: Johns Hopkins Univ Press, 55–58, 1989.

12. Kress, R., *Linear Integral Equations*, Applied Mathematical Sciences, Berlin, MD: Springer-Verlag, 221, 1989.
13. Miller, E. K., "A computational study of the effect of matrix size and type, condition number, coefficient accuracy and computational precision on matrix-solution accuracy," in *IEEE Antennas Propagat. Soc. Int. Symp. Dig.*, Newport Beach, CA, 1020-1023, June 1995.
14. Zhang, D., Y. Rahmat-Samii, H. R. Fetterman, S. Prakash, R. F. Bunshah, M. Eddy, and J. L. Nilsson, "Application of high T_c superconductors as frequency selective surfaces: experiment and theory," *IEEE Trans. Microwave Theory Technique*, Vol. MTT-41, No. 6/7, 1032-1036, Jun/July 1993.